

# Iterative path integral summation for nonequilibrium quantum transport

S. Weiss<sup>\*1</sup>, R. Hützen<sup>2</sup>, D. Becker<sup>3</sup>, J. Eckel<sup>2</sup>, R. Egger<sup>2</sup>, M. Thorwart<sup>4</sup>

<sup>1</sup>Theoretische Physik, Universität Duisburg-Essen and CENIDE, Lotharstr.1, 47048 Duisburg, Germany

<sup>2</sup>Institut für Theoretische Physik IV, Heinrich-Heine-Universität Düsseldorf, Universitätsstr.1, 40225 Düsseldorf, Germany

<sup>3</sup>Departement Physik, Universität Basel, Klingelbergstrasse 82, 4056 Basel, Switzerland

<sup>4</sup>I. Institut für Theoretische Physik, Universität Hamburg, Jungiusstraße 9, 20355 Hamburg, Germany

Received XXXX, revised XXXX, accepted XXXX

Published online XXXX

**Key words:** molecular quantum transport, molecular junctions, quantum dots, nonequilibrium path integrals, exchange coupling, electron-phonon coupling, Keldysh formalism.

\* Corresponding author: e-mail weiss@thp.uni-due.de, Phone:+49-203-379-2969

We have developed a numerically exact approach to compute real-time path integral expressions for quantum transport problems out of equilibrium. The scheme is based on a deterministic iterative summation of the path integral (ISPI) for the generating function of nonequilibrium observables of interest, e.g., the charge current or dynamical quantities of the central part. Self-energies due to the leads, being nonlocal in time, are fully taken into account within a finite memory time, thereby including non-Markovian effects. Numerical results are extrapolated first to vanishing (Trotter) time discretization and, second, to infinite memory time. The method is applied to nonequilibrium transport through a single-impurity Anderson dot in the first place. We benchmark our results in various regimes of the rich parameter space. In the respective regime of validity, ISPI results are shown to match those of other state-of-the-art methods. Especially, we have chosen the mixed valence regime of the Anderson model to compare ISPI to time dependent density matrix renormalization group (tDMRG) and functional RG calculations. Secondly, we determine the nonequilibrium current  $I(V)$  through a molecular junction in presence of a vibrational mode. We have found an exact mapping of the single impurity Anderson-Holstein

model to an effective spin-1 problem. In analytically tractable regimes, as the adiabatic phonon or weak molecule-lead coupling regime, we reproduce known perturbative results. Studying the crossover regime between those limits shows that the Franck-Condon blockade persists in the quantum limit. At low temperature, the Franck-Condon steps in the  $I(V)$  characteristics are smeared due to nonequilibrium conditions. The third system under investigation here is the magnetic Anderson model which consists of a spinful single-orbital quantum dot with an incorporated quantum mechanical spin-1/2 magnetic impurity. Coulomb interaction together with the exchange coupling of the magnetic impurity with the electron spins strongly influence the dynamics. We investigate the nonequilibrium tunneling current through the system as a function of exchange and Coulomb interaction as well as the real-time impurity polarization. From the real-time evolution of physical observables, we are able to determine characteristics of the time-dependent nonequilibrium current and the relaxation dynamics of the impurity. These examples illustrate that the ISPI technique is particularly well suited for the deep quantum regime, when all time and energy scales are of the same order of magnitude.

Copyright line will be provided by the publisher

**1 Introduction** Small condensed matter systems that behave as transistors have attracted numerous research activities in recent years. When placed in a transport setup,

current and noise measurements are used to determine the properties of the usually strongly correlated quantum mechanical system. In as well as out of thermal equilibrium,

Copyright line will be provided by the publisher

several quantum many-body properties of systems such as quantum dots or single molecule junctions are accessible in experiments [1,2]. By down-scaling electronic transistors to the nanometer scale, quantum dots (QD's) allow to control electronic and/or spin properties of single electrons and might be used to impress and read out information. Single molecules, inheriting also vibrational degrees of freedom, are ideal candidates for such devices since they can rather easily be functionalized such that current switches are implemented in a nanoscale environment [3, 4,5,6,7,8]. Furthermore, a controlled design of functional groups attached to molecules seems in reach. The field of molecular electronics is at the intersection of interdisciplinary research areas, combining chemical and physical properties of molecules. Under nonequilibrium conditions transport through molecules challenges experimentalists as well as theoreticians. Nonequilibrium in this review is referred to as the situation that the Fermi energies, provided by source and drain electrodes and located 'left' and 'right' of the structure, are not equal such that electrons are transferred through the system by tunneling. The voltage is assumed to drop at the nanostructure. In such finite voltage bias situations, many interesting physical effects arise due to the quantum nature of the electrons and their strong Coulomb interaction among each other and/or by their interaction with molecular vibrations or local magnetic moments. Prominent examples are resonant tunneling or the Kondo effect [9,10,11]. Different techniques are used to approach the strong coupling limit. For instance, the regime of low energy, low temperature/bias has been approached by Fermi liquid theory [12], via interpolative schemes [13], using integrability concepts [14], or by the perturbative renormalization group (RG) [15, 16]. A perturbative RG analysis has been performed by Schoeller and König [17]. The nonequilibrium generalization of Wilson's numerical RG approach [18] and of the fRG method [19] have been discussed. Transport features have also been discussed by perturbation theory in the interaction strength [20]. On the other hand, perturbatively treating the tunneling matrix elements is a powerful way of describing the incoherent regime, see Ref. [9]. Density matrix renormalization group techniques have been extended to the nonequilibrium regime [21,22]. In addition the flow equation method allows to study the Toulouse point of the Kondo model [23].

In case that a molecule is placed between electrodes, an appropriate theoretical description is needed to deal with its characteristic vibrational (phonon) degrees of freedom [2,24]. The interplay between mechanical and electronic degrees of freedom is of interest in other areas of physics as well, e.g., for inelastic tunneling spectroscopy [25], nanoelectromechanical systems [26], break junctions [27], and suspended semiconductor or carbon-based nanostructures [28,29,30,31]. Including vibrational degrees of freedom via a simple Anderson Holstein (AH) model, where a spinless electronic level is coupled to a single oscillator

mode, shows several effects as the Franck-Condon blockade, negative differential conductance, or current induced heating or cooling [32,33]; for a review, see Ref. [25]. As for the interacting Anderson model, analytical approaches typically address different corners of parameter space, a full theory that connects those corners seems not in reach at present.

A third topic addressed in this review is the investigation of a magnetic QD. Those setups have been studied experimentally in ensembles which are particularly suited for the investigation by laser and electromagnet fields [34,35,36,37,38,39,40]. They are designed with standard lithographic methods and are technologically well established. Moreover, embedding individual magnetic Mn ions into quantum dots and studying the electrical properties is possible [41,42,43]. Small quantum dots with few charge carriers and a single magnetic impurity may become important candidates for efficient high density spintronic devices.

There is a considerable need for numerical methods which describe small quantum systems out of equilibrium accurately and, ideally, treat simple model Hamiltonians numerically exactly. Numerical renormalization group [44] or quantum Monte Carlo (QMC) calculations [45,46,47, 48,49,50] provide a possible line of attack to those problems. Due to the dynamical sign problem, these calculations become increasingly difficult at low temperatures, but in several parameter regions, the stationary steady-state regime seems accessible. Based on non-standard ensembles, the steady state is described in a recent work by Han [51], using an imaginary-time QMC approach followed by a double analytical continuation scheme. This last step is numerically the most difficult part [52].

We here review the development of a novel numerical scheme denoted as *iterative summation of real-time path integrals* (ISPI), in order to address quantum transport problems out of equilibrium [53]. Many-body systems driven out of equilibrium are known [15,54,55] to acquire a steady state that may be quite different in character from their ground-state properties. Details of the steady state may depend on the nature of the correlations, as well as on the way in which the system is driven out of equilibrium. Our ISPI approach, described in detail below, provides an alternative and numerically exact method to tackle out-of-equilibrium transport in correlated quantum dots. Based on the evaluation of the full nonequilibrium Keldysh generating function, along with the inclusion of suitable source terms, observables of interest are computed. It builds on the fact that nonlocal in time correlations, induced by the fermionic leads, decay exponentially in the long-time limit at any finite temperature. Within a characteristic time  $\tau_c$ , all correlations are taken into account, while for larger times, the correlations are dropped due to their exponentially small contributions. This allows us to construct an iterative scheme to evaluate the generating function. An appropriate extrapolation procedure allows to eliminate the

Trotter time discretization error (the Hubbard-Stratonovich (HS) transformation below requires to discretize time) as well as the finite memory-time error. This yields the desired numerically exact value for the observables of interest. Note that the need for a finite memory time makes our approach difficult to apply at very low energies ( $T, V \rightarrow 0$ ). Fortunately, other methods are available in this regime. At finite  $T$  or  $V$ , the requirement of not too long memory times is exploited and the spin path summation remains tractable. Recently, also Segal et al., see Ref. [56] have provided an alternative formulation of the ISPI approach in terms of Feynman Vernon like influence functionals.

The ISPI scheme is implemented here for three characteristic impurity models. First, the single-level Anderson impurity model [57, 58, 59, 60, 61], second the spinless Anderson Holstein model [25], which mimics the behavior of a molecular quantum dot. Finally, when magnetic molecules are investigated, additional couplings to localized spin impurities are important. Results for the relaxation dynamics of such a system are presented in this article as well.

The present paper is organized as follows. In Sec. 2, we introduce the model for the quantum dot coupled to normal leads. We present the computation of the generating function for the nonequilibrium Anderson model there as well. The presence of an external source term allows to calculate the current as a functional derivative. In Sec. 3 we introduce the numerical iterative path integral summation method, from which we obtain observables of interest. We give a detailed discussion of the convergence properties of our method and describe the extrapolation scheme. For several sets of parameters, we will present results and benchmark checks in Sec. 4. In addition, results for the mixed valence regime of the Anderson model are presented. A good agreement with tDMRG and fRG is found. The Anderson Holstein model is studied by means of the ISPI method in Sec. 5, the main finding of a sustained Franck-Condon blockade at low temperatures is discussed upon validating our spin-1 mapping of the AH Hamiltonian. By far the most complex model of this work, a magnetic interacting QD is studied in Sec. 6. We briefly review the necessary changes in the appearing Keldysh generating function and discuss our results on the relaxation time and impurity polarization as well as the tunneling current. A summary is given in Sec. 7.

## 2 Keldysh generating function for non-interacting impurity models

We consider the generic Hamiltonian for a quantum dot that is coupled to metallic leads to the left and right side ( $\hbar = 1, k_B = 1$ )

$$\begin{aligned} \mathcal{H} &= H_{dot} + H_{leads} + H_T \\ &= \sum_{\sigma} E_{0\sigma} n_{\sigma} + \sum_{kp\sigma} (\epsilon_{kp} - \mu_p) c_{kp\sigma}^{\dagger} c_{kp\sigma} \\ &\quad - \sum_{kp\sigma} \left[ t_p c_{kp\sigma}^{\dagger} d_{\sigma} + h.c. \right]. \end{aligned} \quad (1)$$

Here,  $E_{0\sigma} = E_0 + \sigma B$  with  $\sigma = \uparrow, \downarrow = \pm$  is the energy of a single electron with spin  $\sigma$  on the isolated dot. Tuning a back gate voltage or a Zeeman magnetic field term  $\propto B$  changes the value of  $E_{0\sigma}$ . The latter is assumed not to affect the electron dispersion in the leads. The corresponding dot electron annihilation/creation operator is  $d_{\sigma}/d_{\sigma}^{\dagger}$ , with the density operator  $n_{\sigma} \equiv d_{\sigma}^{\dagger} d_{\sigma}$ . Possible eigenvalues of  $n_{\sigma}$  are  $\nu = 0, 1$ , corresponding to the empty or occupied electronic state with spin  $\sigma$ . Interactions on the quantum dot are treated in Sec. 2.1 and not considered for the moment. In Eq. (1),  $\epsilon_{kp}$  denotes the energies of the noninteracting electrons (operators  $c_{kp\sigma}$ ) in lead  $p = L/R = \pm$ , with chemical potential  $\mu_p = peV/2$ . Quantum dot and leads are connected by the tunnel couplings  $t_p$ . The observable of interest is the (symmetrized) tunneling current  $I = (I_L - I_R)/2$ ,

$$I(t) = -\frac{ie}{2} \sum_{kp\sigma} \left[ pt_p \langle d_{\sigma}^{\dagger} c_{kp\sigma} \rangle_t - pt_p^* \langle c_{kp\sigma}^{\dagger} d_{\sigma} \rangle_t \right], \quad (2)$$

where  $I_p(t) = -e\dot{N}_p(t)$  with  $N_p(t) = \langle \sum_{k\sigma} c_{kp\sigma}^{\dagger} c_{kp\sigma} \rangle_t$ . The stationary steady-state dc current follows as the asymptotic long-time limit,  $I = \lim_{t \rightarrow \infty} I(t)$ . We have explicitly confirmed that current conservation,  $I_L + I_R = 0$ , is numerically fulfilled for the ISPI scheme.

In the presence of a finite bias voltage,  $V \neq 0$ , the Keldysh technique [62, 63, 64] provides a way to study nonequilibrium transport. In this formalism, the time axis is extended to a contour with  $\alpha = \pm$  branches, see Ref. [64], along with an effective doubling of fields. The Keldysh Green function (GF) exhibits a matrix structure  $G_{ij}^{\alpha\beta}(t_{\alpha}, t'_{\beta}) = -i \langle \mathcal{T}_C [\psi_i(t_{\alpha}) \psi_j^{\dagger}(t'_{\beta})] \rangle$ , where  $\mathcal{T}_C$  denotes the contour ordering of times along the Keldysh contour, and  $i, j = L, R, 0$  correspond to fields representing lead or dot fermions, respectively. We omit the spin indices here, remembering that each entry still is a diagonal  $2 \times 2$  matrix in spin space. The Keldysh partition function contains all relevant information about the physics of the system. In order to obtain it, we first integrate over the noninteracting lead fermion fields. Subsequently, we integrate over the dot fields as well. In a fermion coherent state basis, the generating function is

$$Z[\eta] = \int \mathcal{D} \left[ \prod_{\sigma} \bar{d}_{\sigma}, d_{\sigma}, \bar{c}_{kp\sigma}, c_{kp\sigma} \right] e^{iS[\bar{d}_{\sigma}, d_{\sigma}, \bar{c}_{kp\sigma}, c_{kp\sigma}]}, \quad (3)$$

with Grassmann fields  $(\bar{d}_{\sigma}, d_{\sigma}, \bar{c}, c)$ . The external source term, which allows to compute the current at measurement time  $t_m$ , is chosen such that

$$I(t_m) = -i \frac{\partial}{\partial \eta} \ln Z[\eta] \Big|_{\eta=0}. \quad (4)$$

Correspondingly, it is also possible to evaluate other observables, e.g., the zero-frequency shot noise, by introducing appropriate source terms and performing the corresponding derivatives. The action is  $S = S_{dot} + S_{leads} +$

$S_T + S_\eta$ , see Ref. [53] for the explicit expressions. After integrating over the leads' degrees of freedom, the effective action for the dot becomes nonlocal in time. The generating function for the noninteracting system reads

$$Z_{ni}[\eta] = \int \mathcal{D} \left[ \prod_{\sigma} \bar{d}_{\sigma} d_{\sigma} \right] e^{i(S_{dot,0} + S_{env})} \quad (5)$$

with

$$S_{env} = \int_C dt \int_C dt' \sum_{\sigma} \bar{d}_{\sigma}(t) \left\{ \gamma_L(t, t') + \gamma_R(t, t') + \frac{ie\eta}{2} [\gamma_L(t, t') - \gamma_R(t, t')] \times [\delta(t - t_m) + \delta(t' - t_m)] \right\} d_{\sigma}(t'). \quad (6)$$

For the source term, the physical measurement time  $t_m$  is fixed on the upper (+) branch, hence the (--) Keldysh element of the source term self-energy vanishes. The  $\gamma_p(t, t')$  matrices in Eq. (6) represent the leads, their Fourier transforms in frequency space are explicitly given as  $2 \times 2$  Keldysh matrices

$$\gamma_p(\omega) = i\Gamma_p \begin{pmatrix} 2f(\omega - \mu_p) - 1 & -2f(\omega - \mu_p) \\ 2 - 2f(\omega - \mu_p) & 2f(\omega - \mu_p) - 1 \end{pmatrix}. \quad (7)$$

With the usual assumption that the leads are in thermal equilibrium,  $f(\omega) = 1/(e^{\omega/T} + 1)$ . Taking the wide-band limit with a constant density of states  $\rho(\epsilon_F)$  per spin channel around the Fermi energy, the hybridization  $\Gamma_p = \pi\rho(\epsilon_F)|t_p|^2$  of the dot level with lead  $p$  enters. We focus on symmetric contacts  $\Gamma_L = \Gamma_R \equiv \Gamma/2$  and on symmetrically applied bias voltages as well. The generalization to asymmetric contacts is straightforward.

In the next step (still for vanishing on-dot interactions), we integrate over the dot degrees of freedom. This yields the noninteracting generating function

$$Z_{ni}[\eta] = \prod_{\sigma} \det [iG_{0\sigma}^{-1}(t, t') + \eta\Sigma^J(t, t')]. \quad (8)$$

The function  $G_{0\sigma}^{-1}(t, t')$  follows from

$$G_{0\sigma}(\omega) = [(\omega - \epsilon_{0\sigma})\tau_z - \gamma_L(\omega) - \gamma_R(\omega)]^{-1} = \frac{1}{1 + [(\omega - \epsilon_{0\sigma})/\Gamma]^2} \times \begin{pmatrix} \omega - \epsilon_{0\sigma} + i\Gamma(1 - F) & i\Gamma F \\ i\Gamma(F - 2) & -\omega + \epsilon_{0\sigma} + i\Gamma(1 - F) \end{pmatrix},$$

where  $\tau_z$  is the standard Pauli matrix in Keldysh space, and  $F = f(\omega + eV/2) + f(\omega - eV/2)$ . Moreover, the self-energy for the source term is obtained as

$$\Sigma^J(t, t') = \frac{e}{2} [\gamma_L(t, t') - \gamma_R(t, t')] \times [\delta(t - t_m) + \delta(t' - t_m)]. \quad (9)$$

Up to this point, we have discussed the noninteracting case. The next section describes how to include the electron-electron interaction.

**2.1 Hubbard-Stratonovich transformation** In the presence of on-dot Coulomb interactions, we add the Coulomb term

$$H_{int} = U n_{\uparrow} n_{\downarrow} \quad (10)$$

to the Hamiltonian in Eq. (1). For our purpose, it is convenient to use the operator identity  $n_{\uparrow} n_{\downarrow} = \frac{1}{2}(n_{\uparrow} + n_{\downarrow}) - \frac{1}{2}(n_{\uparrow} - n_{\downarrow})^2$ , which results in a shift of the single-particle energies  $\epsilon_{0\sigma} \equiv E_{0\sigma} + U/2$ , and we may rewrite  $H_{dot} = H_{dot,0} + H_U = \sum_{\sigma} \epsilon_{0\sigma} n_{\sigma} - \frac{U}{2}(n_{\uparrow} - n_{\downarrow})^2$ . Now, the action in Eq. (3) in real time contains quartic terms of dot Grassmann fields and a Gaussian integration is not possible. We will use a time-discrete path integral for the following discussion [65]. In order to decouple the quartic term, we discretize the full time interval,  $t = N\delta_t$ , with the time increment  $\delta_t$ . On each time slice, we perform a Trotter breakup of the dot propagator according to  $e^{i\delta_t(H_0 + H_U)} = e^{i\delta_t H_U/2} e^{i\delta_t H_0} e^{i\delta_t H_U/2} + O(\delta_t^2)$ , where  $H_0 = H_{dot} + H_{leads}$ . According to Refs. [66, 67, 68] the emerging Trotter error can be systematically eliminated from the results [69, 70], see below. On a single Trotter slice, a discrete Hubbard-Stratonovich transformation [67, 71, 72, 73] allows to decouple the interaction. This locally introduces Ising-like discrete spin fields  $s_n = (s_n^+, s_n^-)$  on the  $\alpha = \pm$  branches of the Keldysh contour with  $s_n^{\alpha} = \pm 1$  on the  $n$ -th Trotter slice. For a given Trotter slice, we define

$$e^{\pm i\delta_t U (n_{\uparrow} - n_{\downarrow})^2 / 2} = \frac{1}{2} \sum_{s^{\pm} = \pm} e^{-\delta_t \lambda_{\pm} s^{\pm} (n_{\uparrow} - n_{\downarrow})}. \quad (11)$$

The HS parameter is obtained from the equation,

$$\cosh(\delta_t \lambda_{\pm}) = \cos(\delta_t U/2) \pm i \sin(\delta_t U/2),$$

under the condition that  $U > 0$ , see Ref. [53]. Note that the arbitrarily chosen overall sign of  $\lambda_{\pm}$  does not influence the physical result. Uniqueness of this HS transformation requires  $U\delta_t < \pi$ . To ensure sufficiently small time discretizations, we meet the condition  $\max(U, e|V|, |\epsilon_0|, T) \lesssim 1/\delta_t$  in all calculations in general.

After the HS transformation, the remaining fermionic Grassmann variables ( $\bar{d}_{\sigma}, d_{\sigma}$ ) appear quadratically and are integrated out at the cost of the full path summation over the discrete HS Ising spins  $\{s\}$  according to

$$Z[\eta] = \sum_{\{s\}} \prod_{\sigma} \det G_{\sigma}^{-1}[\{s\}, \eta]. \quad (12)$$

The full Keldysh GF written in time-discretized ( $1 \leq k, l \leq N$ ) form is

$$(G_{\sigma}^{-1})_{kl}^{\alpha\beta}[\{s\}, \eta] = (G_{0\sigma}^{-1})_{kl}^{\alpha\beta} + i\eta \Sigma_{kl}^{J, \alpha\beta} - i\delta_t \delta_{kl} \lambda_{\alpha} s_k^{\alpha} \delta_{\alpha\beta}, \quad (13)$$

where  $\alpha, \beta = \pm$  labels the Keldysh branches, and the non-interacting GF is

$$G_{0\sigma, kl} = \int_{-\infty}^{\infty} \frac{d\omega}{2\pi} e^{i\delta_t(k-l)\omega} G_{0\sigma}(\omega). \quad (14)$$

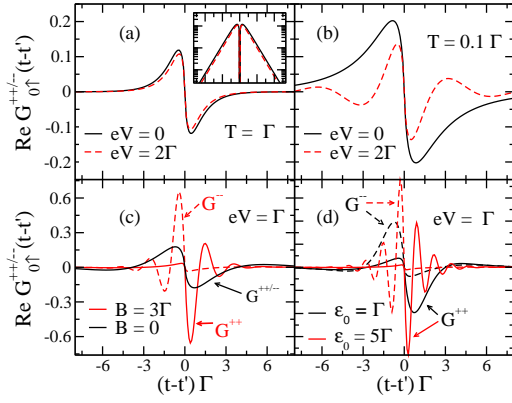


**Figure 1** (Color online) Green's function of the non-interacting quantum dot in the presence of the leads for different settings of gate and bias voltages as well as magnetic field. The inset in (a) shows  $|\text{Re} G_{0\uparrow}^{--}(t-t')|$  in a log-linear representation.

Note that  $G_{0\sigma}(t, t')$  depends only on time differences due to time-translational invariance of the noninteracting part which holds at thermal equilibrium of the leads. The respective time discrete version of the self-energy kernel for the source term is, cf. Eqs. (6) and (9),

$$\Sigma_{kl}^{J,\alpha\beta} = \frac{e}{2} \left[ \gamma_{L,kl}^{\alpha\beta} - \gamma_{R,kl}^{\alpha\beta} \right] \frac{\delta_{mk}\delta_{\alpha,+} + \delta_{ml}\delta_{\beta,+}}{\delta_t}, \quad (15)$$

where  $\gamma_{p,kl} = \gamma_p(t_k - t_l)$  and the measurement time is  $t_m = m\delta_t$ .

**3 Formulation of the iterative scheme** In this section we review the construction for the iterative expressions for the Keldysh partition function which form the ISPI scheme. For this, we exploit the property (see, e.g., Ref. [53,73,74,75]) that each Keldysh component of  $G_{0\sigma}(t-t')$  in Eq. (14) decays exponentially at long time differences ( $\delta_t|k-l| \rightarrow \infty$ ) for any finite temperature, see Eq. (14). The related time scale is denoted as correlation or memory time  $\tau_c$ . In Fig. 1, we show typical examples of  $\text{Re} G_{0\uparrow}^{++/-}(t-t')$  for different bias voltages  $V$ . The exponential decrease with time is presented in the inset of Fig. 1(a), where the absolute value  $|\text{Re} G_{0\uparrow}^{--}(t-t')|$  is plotted in log-linear representation for the same parameters. For large bias voltages and low enough temperatures, e.g., at  $eV \gtrsim \Gamma$  and  $T \leq 0.2\Gamma$ , the decay is superposed by an oscillatory behavior. Since the lead-induced correlation function decays as  $\sim \cos[eV(t-t')/2]/\sinh[\pi T(t-t')]$ , the respective correlations decay on a time scale given by

$\tau_c^{-1} \sim \max(k_B T, eV)$ . Thus, the exponential decay suggests to neglect lead-induced correlations beyond  $\tau_c$ . This motivates an iterative scheme which exactly accounts for correlations within an interval  $\tau_c$ , while neglecting them outside. Notice that the exponential decay is only present

for finite  $T$  and/or  $V$ , whereas at  $T = V = 0$  correlations die out only algebraically, and our approach is not applicable.

Let us then face the remaining path sum in Eq. (12). In the discrete time representation, we denote by  $t_0 = 0 < t_N = N\delta_t$  the initial and final times and  $t_k = k\delta_t$ . The discretized GF and self-energy kernels for given spin  $\sigma$  are then represented as matrices of dimension  $2N \times 2N$ . For explicit calculations, we arrange the matrix elements related to Keldysh space (characterized by the Pauli matrices  $\tau$ ) and to physical times  $(t_k, t_l)$  as  $\tau \otimes (k, l)$ . In particular, the ordering of the matrix elements from left to right (and from top to bottom) follows increasing times. The lead-induced correlations thus decrease exponentially with growing distance from the diagonal of the matrix.

For numerical convenience, we evaluate the generating function in the equivalent form

$$Z[\eta] = \mathcal{N} \sum_{\{s\}} \prod_{\sigma} \det D_{\sigma}[\{s\}, \eta], \quad (16)$$

with  $D_{\sigma} = G_{\sigma}^{-1} G_{0\sigma}$ , see Ref. [53] for details, and thus get

$$D_{\sigma,kl}^{\alpha\beta}[\{s\}, \eta] = \delta_{\alpha\beta} \delta_{kl} + i\delta_t \lambda_{\alpha} G_{0\sigma,kl}^{\alpha\beta} s_k^{\alpha} - i\eta \sum_{j,\alpha'} G_{0\sigma,kj}^{\alpha\alpha'} \Sigma_{jl}^{J,\alpha'\beta}. \quad (17)$$

By construction, we have to sum over  $2N$  auxiliary Ising spins, which appear line-wise. The total number of possible spin configurations is  $2^{2N}$ .

Next, we exploit the truncation of the GF by setting  $D_{kl} \equiv 0$  for  $|k-l|\delta_t > \tau_c$ , where  $\tau_c \equiv K\delta_t$  is the correlation time, with the respective number  $K$  of Trotter time slices. All GF matrices have a band structure whose band width is given by  $K$ . Equivalently, we can use for the spin-spin correlation the definition

$$s_i^{\alpha} \cdot s_j^{\beta} = \begin{cases} s_i^{\alpha} \cdot s_j^{\beta}, & \text{if } |i-j| \leq K, \\ 0, & \text{else.} \end{cases} \quad (18)$$

We note that in the continuum limit, i.e.,  $K = N, \delta_t \rightarrow 0$  and  $N \rightarrow \infty$ , the approach is formally exact.

To proceed, we exploit that the determinant of a quadratic block matrix  $D = \begin{pmatrix} a & b \\ c & d \end{pmatrix}$  is given by  $\det(D) = \det(a) \det(d - ca^{-1}b)$ .

In time space, we obtain the  $(N \times N)$ -Keldysh GF band matrix

$$D \equiv D_{(1, N_K)} = \begin{pmatrix} D^{11} & D^{12} & 0 & 0 & \dots & 0 \\ D^{21} & D^{22} & D^{23} & 0 & \dots & \vdots \\ 0 & D^{32} & D^{33} & D^{34} & \dots & \vdots \\ 0 & 0 & D^{43} & D^{44} & \dots & 0 \\ \vdots & \vdots & \vdots & \vdots & \ddots & D^{N_K-1, N_K} \\ 0 & \dots & \dots & 0 & D^{N_K, N_K-1} & D^{N_K, N_K} \end{pmatrix},$$

where the single blocks are  $(K \times K)$ -block matrices defined as  $(l, l' = 1, \dots, N_K)$

$$D^{ll'} = \begin{pmatrix} D_{(l-1)K+1, (l'-1)K+1} \dots D_{(l-1)K+1, l'K} \\ \vdots & \ddots & \vdots \\ D_{lK, (l'-1)K+1} \dots D_{lK, l'K} \end{pmatrix}.$$

Without loss of generality, the number  $N$  of Trotter slices is chosen as integer such that  $N_K \equiv N/K$  and the matrix elements  $D_{kl}$  follow from Eq. (17). We keep their dependence on the Ising spins  $s_k^\pm$  implicit. Each  $D_{kl}$  still has a  $2 \times 2$ -Keldysh structure and a  $2 \times 2$  spin structure. If we apply the formula for the determinant from above, the generating function (16) is represented as

$$Z[\eta] = \sum_{s_1^\pm, \dots, s_N^\pm} \det \{ D^{11}[s_1^\pm, \dots, s_{N_K}^\pm] \} \\ \times \det \left\{ D_{(2, N_K)}[s_{K+1}^\pm, \dots, s_N^\pm] - D^{21}[s_{K+1}^\pm, \dots, s_{2K}^\pm] [D^{11}[s_1^\pm, \dots, s_{K}^\pm]]^{-1} D^{12}[s_{K+1}^\pm, \dots, s_{2K}^\pm] \right\}, \quad (19)$$

where the  $(N_K - 1) \times (N_K - 1)$ -matrix  $D_{(2, N_K)}$  is obtained from  $D_{(1, N_K)}$  by removing the first line and the first column.

In order to set up an iterative scheme, we use the following observation: to be consistent with the truncation of the correlations after a memory time  $K\delta_t$ , we have to neglect terms that directly couple Ising spins at time differences larger than  $\tau_c$ , see also Eq. (18), consequently matrix products of the form

$$D^{l+2, l+1} [D^{l+1, l+1}]^{-1} D^{l+1, l} [D^{l, l}]^{-1} D^{l, l+1} [D^{l+1, l+1}]^{-1} D^{l+1, l+2} = 0 \quad (20)$$

within the Schur complement in each further iteration step. We do not neglect the full Schur complement but only those parts which are generated in the second-next iteration step. With this, we rewrite the generating function as

$$Z[\eta] = \sum_{s_1^\pm, \dots, s_N^\pm} \det \{ D^{11}[s_1^\pm, \dots, s_{N_K}^\pm] \} \prod_{l=1}^{N_K-1} \det \left\{ D^{l+1, l+1}[s_{lK+1}^\pm, \dots, s_{(l+1)K}^\pm] \right. \\ \left. - D^{l+1, l}[s_{lK+1}^\pm, \dots, s_{(l+1)K}^\pm] [D^{l, l}[s_{(l-1)K+1}^\pm, \dots, s_{lK}^\pm]]^{-1} D^{l, l+1}[s_{lK+1}^\pm, \dots, s_{(l+1)K}^\pm] \right\}. \quad (21)$$

Exchanging the sum and the product, and reordering the sum over all Ising spins, we obtain

$$Z[\eta] = \sum_{s_{N-K+1}^\pm, \dots, s_N^\pm} Z_{N_K}[s_{N-K+1}^\pm, \dots, s_N^\pm], \quad (22)$$

where  $Z_{N_K}$  is the last element obtained from the iterative procedure defined by  $(l = 1, \dots, N_K - 1)$

$$Z_{l+1}[s_{lK+1}^\pm, \dots, s_{(l+1)K}^\pm] = \sum_{s_{(l-1)K+1}^\pm, \dots, s_{lK}^\pm} A_l[s_{(l-1)K+1}^\pm, \dots, s_{lK}^\pm, s_{lK+1}^\pm, \dots, s_{(l+1)K}^\pm] Z_l[s_{(l-1)K+1}^\pm, \dots, s_{lK}^\pm]. \quad (23)$$

The propagating tensor  $A_l$  is read off from Eq. (21) as

$$A_l = \det \left\{ D^{l+1, l+1} [s_{lK+1}^\pm, \dots, s_{(l+1)K}^\pm] \right. \\ \left. - D^{l+1, l} [s_{lK+1}^\pm, \dots, s_{(l+1)K}^\pm] \left[ D^{l, l} [s_{(l-1)K+1}^\pm, \dots, s_{lK}^\pm] \right]^{-1} D^{l, l+1} [s_{lK+1}^\pm, \dots, s_{(l+1)K}^\pm] \right\}. \quad (24)$$

The iteration starts with  $Z_1[s_1^\pm, \dots, s_K^\pm] = \det \{ D^{11} [s_1^\pm, \dots, s_K^\pm] \}$ .

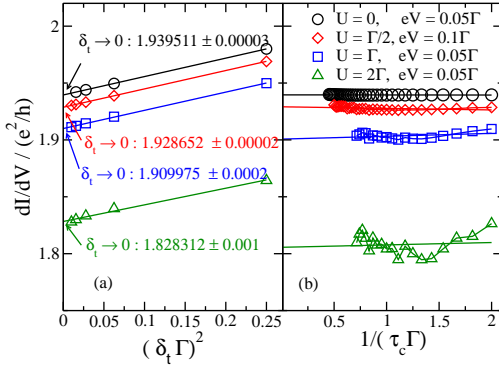


**Figure 2** (Color online) Extrapolation scheme for raw data obtained with ISPI. First the Trotter error, panel (a) and then the memory truncation error (b) are extrapolated. Notice that whenever the ISPI data are converged, they are numerically exact.

The current is numerically obtained by evaluating Eq. (4) for a small but fixed value of  $\eta$ ; we have taken  $\eta = 0.001$  for all results shown. The current as a function of time  $I(t_m)$  shows a transient oscillatory or relaxation behavior at short times. We extract the stationary value  $I$  when the current has saturated to a plateau.

### 3.1 Convergence and extrapolation procedure

By construction there are two systematic errors in the scheme: (i) the Trotter error due to finite time discretization  $\delta_t = t/N$ , and (ii) the memory error due to a finite memory time  $\tau_c = K\delta_t$ . The scheme becomes exact in the limit  $K \rightarrow \infty$  and  $\delta_t \rightarrow 0$ . We can eliminate both errors from the numerical data in the following systematic way: Step 1: We choose a fixed time discretization  $\delta_t$  and a memory time  $\tau_c$ . A reasonable estimate for  $\tau_c$  is the minimum of  $1/|eV|$  and  $1/T$  (see above). With that, we calculate the current  $I(\delta_t, \tau_c)$ , and, if desired, the differential conductance  $dI(\delta_t, \tau_c)/dV$  (the derivative is performed numerically for a small  $\Delta eV = 0.01\Gamma$ ). The calculation is then repeated for different choices of  $\delta_t$  and  $\tau_c$ . Step 2: Next, the Trotter error can be eliminated by exploiting the fact that it vanishes quadratically for  $\delta_t \rightarrow 0$  [66, 67, 68]. For a fixed memory time  $\tau_c$ , we can thus extrapolate and obtain  $dI(\tau_c)/dV = dI(\delta_t \rightarrow 0, \tau_c)/dV$ ,

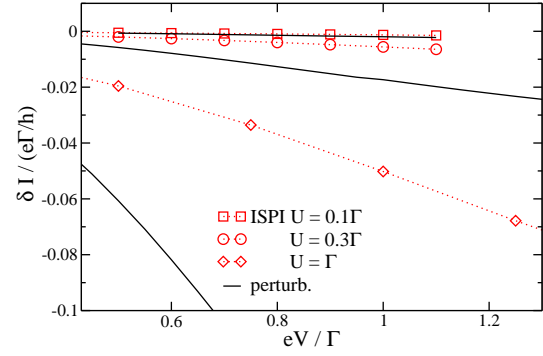


**Figure 3** (Color online) Corrections  $\delta I$  to the current due to finite  $U$  as compared to  $U = 0$  for small to intermediate on-dot interaction  $U \leq \Gamma$ . Other parameters are  $T = 0.1\Gamma$ ,  $\epsilon_0 = B = 0$ . We compare the ISPI data (red symbols) to a 2nd order perturbative calculation, dotted lines guide the eyes.

which still depends on the finite memory time  $\tau_c$ . The quadratic dependence on  $\delta_t$  is illustrated in Fig. 2 (a) for different values of  $U$ . Note that each line corresponds to the same fixed memory time  $\tau_c = 0.5/\Gamma$ . Step 3: In a last step, we eliminate the memory error by extrapolating to  $1/\tau_c \rightarrow 0$ , and obtain the final numerically exact value  $dI/dV = dI(\tau_c \rightarrow \infty)/dV$ . For the dependence on  $1/\tau_c$ , we empirically find a regular and systematic behavior as shown in Fig. 2(b). The  $\tau_c \rightarrow \infty$  value is approached with corrections of the order of  $1/\tau_c$ , see Fig. 2(b).

We have implemented the iterative scheme together with the convergence procedure on standard Xeon 2GHz machines. Computations are then only possible for  $K \leq 7$  due to the limited memory resources available. Typical running times for the shown simulation data are approximately 15 hours for  $K = 5$ .

### 4 Benchmarking the approach: comparison with exact and perturbative results

In this section, we discuss the results obtained for the Anderson model. We measure energies in units of  $\Gamma$ . Unless noted otherwise, all error bars for the shown data points, which are due to the Trotter and memory extrapolation scheme, are of the order of the symbol sizes in the figures.



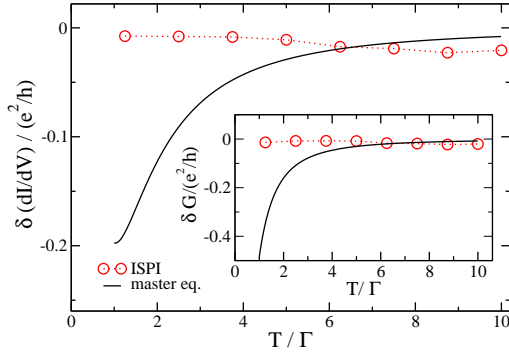


**Figure 4** (Color online) Interaction corrections for  $U = \Gamma$  to the nonlinear (main) and linear conductance (inset) calculated by ISPI (symbols) and by an incoherent rate equation as a function of temperature. In the main panel we have chosen  $eV = 3\Gamma$ .

We stop short on reporting that we have recovered the exact current for the solvable  $U = 0$  case, as a function of the bias and the gate voltage. By construction, the ISPI method includes all tunneling processes exactly to arbitrary orders.

In order to benchmark our code for finite  $U$ , we compare the numerical results to a perturbative calculation at the charge degeneracy point  $\epsilon_0 = B = 0$ , where the interaction self-energy can be computed up to second order in  $U$  [20,76]. For a detailed comparison, we plot mostly the *interaction corrections*,  $\delta A \equiv A(U) - A(U = 0)$ , with  $A$  being the current  $I$ , the linear conductance  $G$ , or the nonlinear conductance  $dI/dV$ , respectively. Figure 3 shows the results for  $\delta I$  as a function of the bias voltage for  $U = 0.1\Gamma$ ,  $U = 0.3\Gamma$  and  $U = \Gamma$ . For  $U = 0.1\Gamma$ , we perfectly recover the perturbative results, which confirms the reliability of our code even in the regime of nonlinear transport. Clearly, the corrections are small and negative, which can be rationalized in terms of indications of Coulomb blockade physics, as transport is suppressed by a finite on-dot interaction. For  $U = 0.3\Gamma$ , the current decreases even further, and the deviations between the ISPI and perturbative results increase. The relative deviation for  $U = 0.3\Gamma$  is already  $\approx 30 - 35\%$ , illustrating that perturbation theory is already of limited accuracy in this regime. Although it well reproduces the overall tendency, there is a significant quantitative difference. It is even more pronounced for  $U = \Gamma$ , as shown in the figure. Here, second-order perturbation theory does not even reproduce qualitative features.

**4.1 Comparison with a master equation approach** Next, we compare our numerically exact results with the outcome of a standard classical rate equation calculation [9,58]. The rate equation is expected to yield

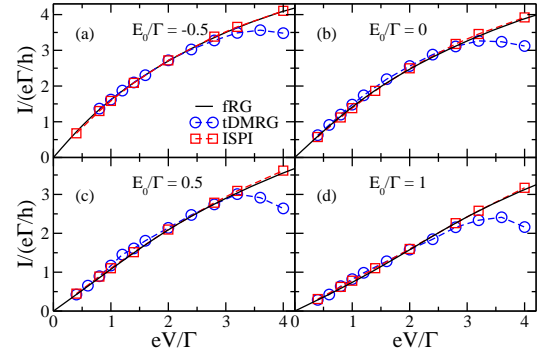


**Figure 5** (Color online) Comparison of ISPI and RG methods in the mixed valence regime. Parameters are chosen as  $U/\Gamma = 2$  and the temperature is  $T = 0.1\Gamma$ . The RG data are taken from Ref. [75]

reliable results in the incoherent (sequential) tunneling regime, when  $T \gg \Gamma$ . Then, a description in terms of occupation probabilities for the isolated many-body dot states is appropriate. Results for  $U = \Gamma$  are shown in Fig. 4, both for the interaction corrections to the nonlinear and the linear conductance. When the temperature is lowered,  $T < \Gamma$ , quantum coherent interaction effects become more important, as seen from the exact ISPI results. They are clearly not captured by the master equation in the sequential tunneling approximation. However, for  $T \gg \Gamma$ , interaction corrections are washed out, and the master equation becomes accurate, cf. Fig. 4. Similarly, from our ISPI results, we have found (data not shown) that interaction corrections are suppressed by an increasing bias voltage as well.

**4.2 ISPI vs. tDMRG and fRG** The mixed valence regime is characterized by the fact that the QD's occupation fluctuates between the different charge states, namely empty, singly and doubly occupied, see Ref. [77] for details. Furthermore the coupling to the leads is strong, i.e. the Kondo temperature  $T_K \sim \Gamma$ , see below in Sec. 4.3. When controlling the gate voltage by tuning  $\epsilon_0$ , it is possible to tune the nanostructure into this limit. From the theoretical point of view another energy scale  $\epsilon_0$  enters, again, not as a small parameter and simulation methods are rare in this regime. For the case of intermediate Coulomb repulsion  $U/\Gamma = 2$  we have studied [75] the mixed valence regime and compare our results to other state-of-the-art methods, functional renormalization group (fRG) [19] and time dependent density matrix renormalization group (tDMRG)[21,22]. The results are shown in Fig. 5 for the steady state current  $I(V)$  for  $\epsilon_0 \neq 0$ , i.e., away from the charge degeneracy point. The results from fRG and ISPI match perfectly from small bias voltages  $eV/\Gamma \approx 0.2$  up to the strong non-equilibrium regime. We note that by



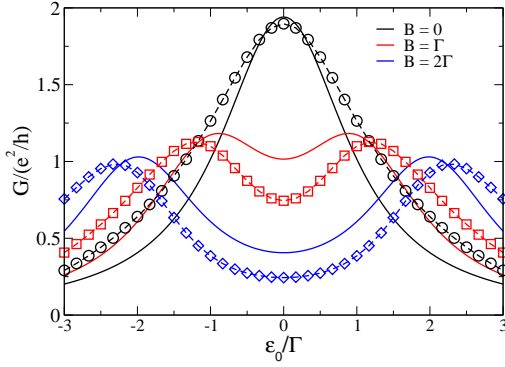


**Figure 6** (Color online) Linear magneto-conductance as a function of the gate voltage  $\epsilon_0$  and  $U = \Gamma$ . The bias voltage is chosen as  $eV = 0.05\Gamma$  and  $T = 0.1\Gamma$ . ISPI data (symbols) are connected by dashed lines as guide to the eyes. The full lines show the analytical results for vanishing interaction  $U \rightarrow 0$ . Finite magnetic fields split the resonant tunneling peak.

construction, it becomes increasingly cumbersome (and finally impossible) to obtain converged ISPI results in the limit of vanishing bias voltages and low temperatures [53], since then the correlations do not decay sufficiently to be truncated. In the present setup, tDMRG has a tendency to overestimate the currents in the mixed valence regime, see Ref. [78] for details, hence we find slight deviations between tDMRG and the two other methods (see  $eV \approx 1.5\Gamma$ , lower left panel). Overall agreement away from the symmetric point between the three methods is very good. Furthermore,  $I(V)$  curves show agreement for a wide range of magnetic fields, applied to the QD, see Ref. [75] for details.

**4.3 Small bias regime  $eV \ll \Gamma$ :** For sufficiently small bias voltage, the current is linear in  $V$ , and we can focus on the linear conductance  $G$ . Figure 6 shows  $G(\epsilon_0)$  for different magnetic fields  $B$ , taking  $U = \Gamma$  and  $T = 0.1\Gamma$  (for  $eV = 0.05\Gamma$ ). For  $B = 0$ , two spin-degenerate transport channels contribute, and a single resonant-tunneling peak at  $\epsilon_0 = 0$  results. For  $B \neq 0$ , the spin-dependent channels are split by  $\Delta\epsilon_0 = 2B$ , resulting in a double-peak structure. Furthermore, since also  $U$  lifts the degeneracy, the spin-resolved levels are now located at  $\epsilon_0 = \pm(B + U/2)$  due to the Zeeman splitting. We find an interaction-induced broadening, cf. Fig. 6, of the resonant-tunneling peak as compared to the noninteracting case. The width of the Lorentzian peak profile for  $B = 0$  is determined by  $\Gamma$  at sufficiently low  $T$ , and broadens as  $T$  increases. Here, the double-peak structure, with two clearly separated peaks for finite  $B$ , is not yet fully developed. The two peaks largely overlap, and the distance of the peaks is below the expected  $\Delta\epsilon_0 = 2B$ , since tunneling significantly broadens the dot levels.

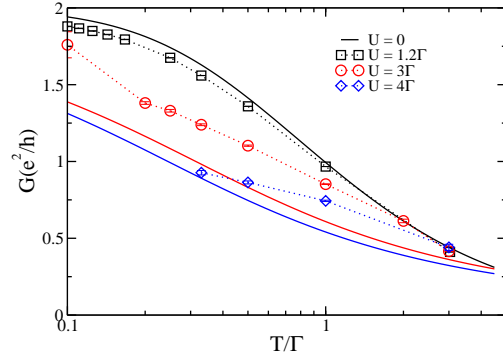


**Figure 7** (Color online) Log-linear plot of the linear conductance  $G$  as a function of temperature. Above and close to the Kondo temperatures  $T_K$ , the ISPI simulation results (symbols) agree with the results of Ref. [79] given as full lines, see text.

Next, we address the temperature dependence of the linear conductance (numerically evaluated for  $eV = 0.05\Gamma$ ). In Fig. 7, we show  $G(T)$  for different values of  $U$  (up to  $U = 4\Gamma$ ) at  $\epsilon_0 = B = 0$ . For  $U = 1.2\Gamma$ , the deviations from the  $U = 0$ -result is small. For larger  $U$ , deviations become more pronounced at low temperatures where the on-dot interaction becomes increasingly relevant. Up to present, we have obtained converged results in the regime of *small* bias voltages for interaction strengths  $U \leq 4\Gamma$  for temperatures above or close to the Kondo temperature,  $T \gtrsim T_K$ . The corresponding Kondo temperatures are  $T_K = 0.38\Gamma$  for  $U = 3\Gamma$  and  $T_K = 0.293\Gamma$  for  $U = 4\Gamma$ . In the regime  $T_K \lesssim T \lesssim 10T_K$ , we compare our results to the result of Hamann [77, 79],

$$G(T) = \frac{e^2}{h} \left( 1 - \frac{\ln(T/T_{KH})}{[\ln^2(T/T_{KH}) + 3\pi^2/4]^{1/2}} \right), \quad (25)$$

for the linear conductance, where  $T_{KH} = T_K/1.2$ , see Fig. 7 (solid lines). In Ref. [77], it has been shown that the results of the numerical RG coincide with those of Eq. (25) in this regime. Fig. 7 illustrates that the agreement between the two approaches is satisfactory and shows that the ISPI provides reliable results in the linear regime above or close to the Kondo temperature. Due to the construction of the approach, the situation is more favorable for large bias voltages, where short to intermediate memory times allow us to obtain convergent results.

**4.4 Large bias regime  $eV \geq \Gamma$ :** Let us then turn to nonequilibrium transport for voltages  $eV \gtrsim \Gamma$ . Here, the transport window is given by  $\sim eV$ , and a double-peak structure for  $dI/dV$  emerges even for  $B = 0$ , see Fig. 8 with distance  $eV$  between the peaks. We show results for  $eV = 3\Gamma$  but otherwise the same parameters as in Fig. 6. For an additional finite magnetic field, each peak of the

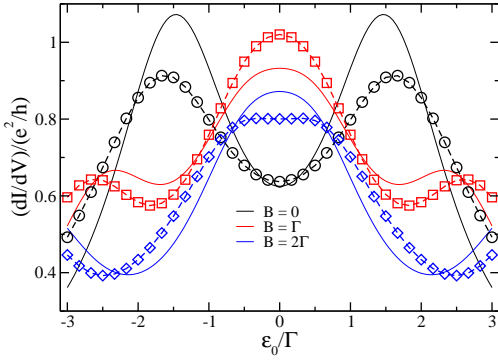


**Figure 8** (Color online) Same as in Fig. 6 but for a large bias voltage  $eV = 3\Gamma$ .

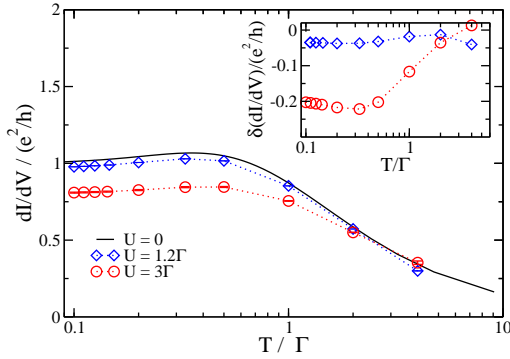


**Figure 9** (Color online) Log-linear representation of the temperature dependence of the differential conductance for different interaction strengths  $0 \leq U/\Gamma < 3$  for  $eV = 2\Gamma$ ,  $\epsilon_0 = B = 0$ .

double-peak structure itself experiences an additional Zeeman splitting, resulting in an overall four-peak structure. For  $B = \Gamma$  and the depicted values of  $U = \Gamma$ , the two innermost peaks (closest to  $\epsilon_0 = 0$ ) overlap so strongly that they effectively form a single peak at  $\epsilon_0 = 0$  again. The two outermost peaks are due to the combination of the finite magnetic field and the bias voltage.

Increasing the on-dot interaction  $U$  downsizes the differential conductance peaks as compared to the noninteracting case, i.e., the interaction corrections are again largest when the level energy matches the chemical potential in the leads. Note that the four-peak structure is already present in the noninteracting case (with  $B \neq 0$ ) and, hence, is not modified qualitatively by a finite  $U$ .

Finally, we address the temperature dependence of the differential conductance  $dI/dV$ . ISPI results for  $eV =$

$2\Gamma$ ,  $\epsilon_0 = B = 0$  are shown in Fig. 9. Again, as in the linear regime, the conductance increases with lower temperatures, and finally saturates, e.g., at  $dI/dV = e^2/h$  for  $U = 0$  and  $eV = 2\Gamma$ . Clearly the conductance decreases when the bias voltage is raised. Increasing  $U$  renders this suppression yet more pronounced, see also inset of Fig. 9 for the corresponding corrections. At high temperatures, thermal fluctuations wash out the interaction effects, and the interaction corrections die out.

**5 Sustained Franck-Condon blockade in molecular quantum dots** As a second example, we apply the ISPI scheme to investigate vibrational effects in the nonequilibrium tunneling current through a molecular quantum dot, see Ref. [73]. We extend the single-impurity Anderson model by a linear phonon of frequency  $\Omega$  (annihilation operator  $b$ ) which couples to a single spinless electronic level with energy  $E_0$  (operators  $d/d^\dagger$ ). Hence, we have the molecular Hamiltonian

$$H_m = \Omega b^\dagger b + [E_0 + \lambda(b + b^\dagger)] n_d \quad (26)$$

with electron-phonon coupling strength  $\lambda$  and  $n_d = d^\dagger d$ .

The short-time propagator on the forward/backward branch of the Keldysh contour,  $e^{\mp i\delta_t H}$ , then allows for a Trotter breakup,  $e^{\mp i\delta_t H} = e^{\mp i\delta_t H_1} e^{\mp i\delta_t (H - H_1)}$ , with  $H_1 = H_m - \Omega b^\dagger b$ , where the auxiliary relation

$$e^{\mp i\delta_t H_1} = 1 - n_d + n_d e^{-\lambda^2 \delta_t^2 / 2} e^{\mp i\delta_t E_0} e^{\mp i\delta_t \lambda b^\dagger} e^{\mp i\delta_t \lambda b} \quad (27)$$

holds. This effectively decouples the electron-phonon interaction in terms of a three-state variable  $s_\eta = 0, \pm 1$  defined at each (discretized) time step  $t_j$  along the forward/backward ( $\alpha = \pm$ ) part of the Keldysh contour, where  $\eta = (t_j, \alpha)$ . Below, we also use the notation  $\eta \pm 1 = (t_{j\pm 1}, \alpha)$  with periodic boundary conditions on the Keldysh contour. The ‘‘Ising spin’’ variable  $s_\eta$  picks up the three terms in Eq. (27) and acts like a Hubbard-Stratonovich auxiliary field, similar to the Ising field employed in the Hirsch-Fye formulation of the Anderson model [53,66,67,68]. The bosonic (phonon) scalar field and the fermionic (dot and lead electrons) Grassmann fields appearing in the Keldysh path integral are noninteracting but couple to the time-dependent auxiliary spin variable. Hence, those fields can be integrated out analytically and the time-dependent current  $I(t_m)$  follows from a path summation as above in Sec. 2. The resulting matrix  $D_{\eta\eta'}$  (in time and Keldysh space) depends on the complete spin path  $\{s\}$ . Specifically, we obtain  $D = -iB(G_d^{-1} - \Sigma)$ , where  $G_d^{-1}$  has spin-dependent matrix elements  $[-iG_d^{-1}]_{\eta+1,\eta} = -s_\eta$ . We find  $\Sigma_{\eta\eta'} \neq 0$  only when  $s_\eta = \pm 1$ , where it coincides with the usual (wide-band limit) expression [80]. Finally, the diagonal matrix  $B$  (quoted here for  $\epsilon_0 = 0$ ) with

$$B_{\eta\eta} = A_{s_\eta} e^{-\lambda^2 \delta_t^2 \sum_{\eta'} \alpha \alpha' [iG_{ph}]_{\eta,\eta'+1} |s_\eta s_{\eta'}|} \quad (28)$$

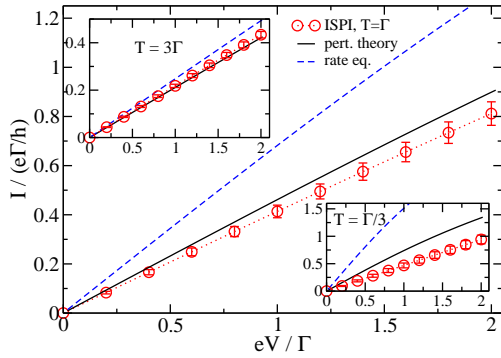


**Figure 10** (Color online) Current  $I$  (in units of  $e\Gamma/h$ ) vs bias voltage  $V$  for the spinless Anderson Holstein model for  $\lambda = 0.5\Gamma$ ,  $\Omega = \Gamma$ ,  $E_0 = 0$ , and  $T = \Gamma$ . The ISPI data are depicted as red circles, where the dotted red curve is a guide to the eyes only and the error bars are explained in the main text. We also show the results of a perturbation theory in  $\lambda$  (solid black curve) and of the rate equation (dashed blue curve). The upper (lower) inset shows the corresponding result for  $T = 3\Gamma$  ( $T = \Gamma/3$ ).

encapsulates all phonon effects, where  $G_{ph}$  is the discretized phonon Green's function, see Ref. [81], and we have used the notation  $A_0 = 1$  and  $A_{\pm 1} = \pm(1/2)e^{-\lambda^2\delta_t^2/2}$ . We comment shortly on the peculiar convergence properties of the present model. Convergence of the extrapolation requires intermediate  $T$  or  $V$ -values, for otherwise the necessary memory times become exceedingly long. For the results below, we have used  $K \leq 4$  and  $0.3 \leq \Gamma\delta_t \leq 0.35$ . The shown current follows by averaging over the  $\delta_t$ -window, with error bars indicating the mean variance. Additional ISPI runs for  $0.18 \leq \Gamma\delta_t \leq 0.22$  and  $0.3 \leq \Gamma\delta_t \leq 0.4$  were consistent with these results, and we conclude that small error bars indicate that convergence has been reached. When dealing with  $3^{2K}$  summands in the evaluation of the generating function in the AH case as compared to  $2^{2K}$  summands for the Anderson model, our ISPI code to calculate  $I(\delta_t, K)$  runs for  $\approx 11$  CPU hours on a 2.93 GHz Xeon processor.

Here, we have once more convinced ourselves that the numerical ISPI results for the  $I(V)$  curves are consistent with known analytical theory in the respective parameter limits. We employ the following perturbative methods: (i) For  $\lambda/\Gamma \ll 1$ , perturbation theory in the electron-phonon coupling applies and yields a closed  $I(V)$  expression for arbitrary values of all other parameters [82]. We note that the solution of the AH model with a very broad dot level [83,84] corresponds to this small- $\lambda$  regime. (ii) For high temperatures,  $T \gg \Gamma$ , a description in terms of a rate equation is possible [80]. We here use the sequential tunneling approximation with golden rule rates [85]. For small  $\lambda$ , the

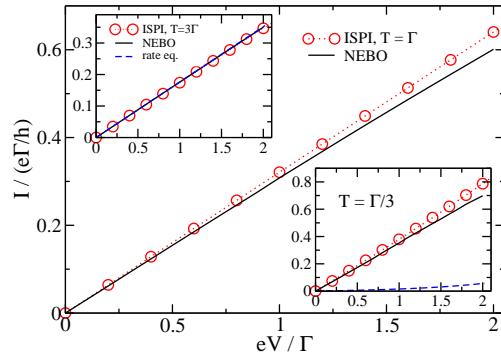


**Figure 11** (Color online) Same as Fig. 10 but for  $\Omega = 0.5\Gamma$  and  $\lambda = \Gamma$ . The main panel is for  $T = \Gamma$  and compares the ISPI results to NEBO predictions. The insets are for  $T = 3\Gamma$  and  $T = \Gamma/3$ , respectively, where also the rate equation results are shown. Notice that in contrast to ISPI, the rate equation predicts an unphysical current blockade for  $T = \Gamma/3$ .

corresponding results match those of perturbation theory, while in the opposite strong-coupling limit, the Franck-Condon blockade occurs and implies a drastic current suppression at low bias voltage [30,86]. (iii) For small oscillator frequency,  $\Omega \ll \min(\Gamma, eV)$ , the nonequilibrium Born-Oppenheimer (NEBO) approximation is appropriate and allows us to obtain  $I(V)$  from a Langevin equation for the oscillator [87,88]. For small  $\lambda$ , this approach is also consistent with perturbative theory, while for high  $T$ , NEBO and rate equation results are found to agree. For clarity, we focus on a resonant level with  $E_0 = 0$  here. The case of weak electron-phonon coupling,  $\lambda = 0.5\Gamma$  is shown Fig. 10. We compare our ISPI data for  $\Omega = \Gamma$  to the results of perturbation theory in  $\lambda$  and of the rate equation. Perturbation theory essentially reproduces the ISPI data. The rate equation is quite accurate for high temperatures, but quantitative agreement with ISPI was obtained only for  $T \gtrsim 10\Gamma$ . We note that the ISPI error bars increase when lowering  $T$  due to the growing memory time ( $\tau_c$ ) demands.

Next, Fig. 11 shows ISPI results for a slow phonon mode,  $\Omega = \Gamma/2$ , with larger electron-phonon coupling  $\lambda = \Gamma$ . In that case, perturbation theory in  $\lambda$  is not reliable and likewise, the rate equation is only accurate at the highest temperature ( $T = 3\Gamma$ ) studied, cf. the upper left inset of Fig. 11. However, we observe from Fig. 11 that for such a slow phonon mode, NEBO provides a good approximation for all temperatures and/or voltages of interest. We conclude that the ISPI technique is capable of accurately describing three different analytically tractable parameter regimes.

In the limit of strong electron-phonon coupling  $\lambda$ , the classical rate equation predicts a Franck-Condon block-

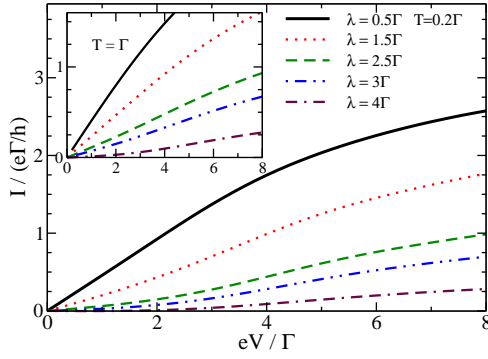


**Figure 12** (Color online) ISPI data for the  $I(V)$  curves for the spinless Anderson Holstein model from weak ( $\lambda = 0.5\Gamma$ ) to strong ( $\lambda = 4\Gamma$ ) electron-phonon coupling, with  $\Omega = 2\Gamma$ . The main panel is for  $T = 0.2\Gamma$ , the inset for  $T = \Gamma$ . We used a dense voltage grid yielding smooth  $I(V)$  curves. Error bars are not shown but remain small, cp. Fig. 10.

ade of the current for low bias and  $T \gg \Gamma$  [86]. Sufficiently large  $\lambda$  can be realized experimentally, and the Franck-Condon blockade has indeed been observed in suspended carbon nanotube quantum dots [30]. For a nonequilibrium phonon with intermediate-to-large  $\lambda$ , understanding the Franck-Condon blockade in the quantum coherent regime of low temperature,  $T < \Gamma$ , is an open theoretical problem. Here, multiple phonon excitation and deexcitation effects generate a complicated (unknown) nonequilibrium phonon distribution function, and the one-step tunneling interpretation in terms of Franck-Condon factors between shifted oscillator parabolas [86] is no longer applicable. We here study this question using ISPI simulations, which automatically take into account quantum coherence effects. In Fig. 12, the crossover from weak to strong electron-phonon coupling  $\lambda$  is considered. The inset shows  $I(V)$  curves for  $T = \Gamma$ , where we observe a current blockade for low voltages once  $\lambda \gtrsim 2\Gamma$ . The blockade becomes more pronounced for increasing  $\lambda$  and is lifted for voltages above the polaron energy  $\lambda^2/\Omega$  [86]. Remarkably, the Franck-Condon blockade persists and becomes even sharper as one enters the quantum-coherent regime (here,  $T = 0.2\Gamma$ ), despite of the breakdown of the sequential tunneling picture. We also observe a nonequilibrium smearing of phonon step-like features in the  $I(V)$  curves in Fig. 12, cf. also Refs. [30, 86].

**6 Nonequilibrium quantum dynamics in the magnetic Anderson model** The third example to which we have applied the ISPI scheme [74] is the magnetic Anderson model. We extend the Hamiltonian Eq. (1) in the presence of Coulomb interactions, see Eq. (10), by a magnetic

impurity localized on the quantum dot which interacts via an exchange interaction with the spins of the confined electrons on the QD. The magnetic part of the Hamiltonian reads

$$H_{imp} + H_{int}^J = \frac{\Delta_{imp}}{2} \tau_z + \underbrace{J \tau_z (d_{\uparrow}^{\dagger} d_{\uparrow} - d_{\downarrow}^{\dagger} d_{\downarrow})}_{H_{int}^{\parallel}} + \underbrace{\frac{J}{2} (\tau_+ d_{\downarrow}^{\dagger} d_{\uparrow} + \tau_- d_{\uparrow}^{\dagger} d_{\downarrow})}_{H_{int}^{\perp}}. \quad (29)$$

The generating function  $\mathcal{Z}[\eta]$  is obtained by integrating again over the corresponding Grassmann fields for dot and lead operators as well as the discrete paths  $\{\tau\}$  and  $\{\zeta\}$  for the real spin variables and the HS Ising fields, respectively, and

$$\mathcal{Z}[\eta] = \sum_{\{\tau, \zeta\}} \int \mathcal{D}[\bar{c}_{kp\sigma} \bar{d}_{\sigma} c_{kp\sigma} d_{\sigma}] (-1)^{\ell} \left( -\frac{iJ\delta_t}{2} \right)^m P[\{\tau\}] e^{iS}. \quad (30)$$

The path sums over impurity and HS spin-fields are performed over the  $2N$ -tuples  $\{\tau_j\} = (\tau_{2N}, \dots, \tau_1)$  and  $\{\zeta_j\} = (\zeta_{2N}, \dots, \zeta_1)$  with  $\tau_j, \zeta_j = \pm 1$ . Within an impurity path  $\{\tau\}$ ,  $m$  flip-flop transitions occur on the Keldysh contour, where  $\ell$  of them lie on the lower branch. The action  $S$  includes tunneling and lead effects as in Eq. (6). Correspondingly, the magnetic part of the action is

$$S_{imp} = -\frac{\Delta_{imp} \delta_t}{2} \sum_{k=2}^N (\tau_k - \tau_{2N-k+1}) = -\frac{\Delta_{imp}}{2} \int_{\mathcal{K}} dt \tau(t). \quad (31)$$

The polynomial  $P[\{\tau\}]$  in Eq. (30) depends on the impurity path  $\{\tau\} = \{\tau^+\}(\{\tau^-\})$  for the forward (backward) branch of the contour. Then, we collect all indices of the flips into the tuple  $T_{\text{flip}}^+ = (k_{m-\ell}^+, \dots, k_1^+)$  (sorted in ascending order) along the forward path  $\{\tau^+\} := (\tau_N, \dots, \tau_1)$  with  $\tau_{k^+} \neq \tau_{k^+-1}$  for all  $k^+ \in T_{\text{flip}}^+$ . Accordingly,  $T_{\text{flip}}^- = (k_{\ell}^-, \dots, k_1^-)$  is the tuple of ascending flip indices along the backward path  $\{\tau^-\} := (\tau_{2N}, \dots, \tau_{N+1})$  with  $\tau_{k^-} \neq \tau_{k^--1}$  for all  $k^- \in T_{\text{flip}}^-$ . Note that a flip index on the backward path is labelled according to the *smaller* step index of the flipping spins corresponding to the *later* time. The impurity polynomial can be expressed in terms of the electronic Grassmann fields as

$$P[\{\tau\}] := \prod_{j \in T_{\text{flip}}^-} \bar{d}_{\tau_j}^{j+1} d_{-\tau_j}^j \prod_{k \in T_{\text{flip}}^+} \bar{d}_{-\tau_k}^k d_{\tau_k}^{k-1}. \quad (32)$$

Figure 13 illustrates an example of an impurity path. Collecting all pieces, the remaining formally exact expression for the Keldysh generating function is

$$\mathcal{Z}[\eta] = \sum_{\{\tau, \zeta\}} \langle P[\{\tau\}] \rangle \prod_{\sigma} \det\{(iG_{\sigma}^{\text{eff}}[\{\tau, \zeta\}, \eta])^{-1}\}. \quad (33)$$



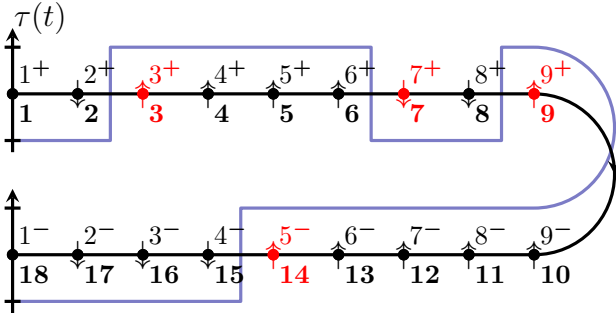


**Figure 13** Exemplary impurity Keldysh path (blue line). The Keldysh contour is divided into  $N - 1 = 8$  segments of length  $\delta_t$  between  $2N = 18$  time vertices. The impurity path (tuple of black and red arrows) realizes  $m = 4$  flip-flops along the contour.

The Keldysh partition function is given as a sum over expectation values of the polynomial  $P$  of Grassmann numbers in a system with Green's function  $G_\sigma^{\text{eff}}$ . In passing, we note that it is possible to express the expectation values for the polynomials  $P$  in terms of Green's functions for the interacting system. The details are given in Ref. [74]. After applying Wick's theorem we obtain explicit expressions for the polynomial [74]. Using matrix elements  $(\Xi_\sigma)_{k,l} = -i\langle d_\sigma^{q_k} \bar{d}_\sigma^{r_l} \rangle = (G_\sigma^{\text{eff}})_{q_k r_l}$ , the final expression for the generating function follows as

$$\mathcal{Z}[\eta] = \lim_{\delta_t \rightarrow 0} \sum_{\{\tau, \zeta\}} (-1)^\ell \left( \frac{J\delta_t}{2} \right)^m \times \exp\{iS_{\text{imp}}\} \prod_{\sigma} \det i(G_\sigma^{\text{eff}})^{-1} \det \Xi_\sigma, \quad (34)$$

where the summation over impurity paths is restricted to tuples  $\{\tau\}$  with  $\tau_1 = \tau_{2N} = \tau_i$ , i.e., correct boundary conditions along the Keldysh contour are fulfilled. The limit  $\delta_t \rightarrow 0$  appears explicitly here, since there is no continuous measure used for the discrete spin paths, neither for the HS- nor for the impurity spins. In order to reduce the exponentially growing number of contributing paths ( $\sim 4^K$ , due to real spin and HS spins) without affecting the accuracy, we may exploit that the propagating tensor depends on the number  $m_j$  of flip-flops in path segment  $j$  and  $0 \leq m_j \leq 2(K-1)$  along the Keldysh contour. We observe that the weight of each segment is smaller, the more flip-flops it contains. On the other hand, the number of path segments  $\{\tau\}_j$  with  $m_j$  flip-flops (given by  $4C_{m_j}^{2(K-1)}$  with  $C_k^n = n!/[k!(n-k)!]$ ) grows as long as  $0 \leq m_j \leq K-1$ , but decreases again when  $K \leq m_j \leq 2(K-1)$ . As a consequence, for any observable there exists a maximal  $m_j^{\text{max}}$  such that contributions from paths with  $m_j > m_j^{\text{max}} \leq 2(K-1)$  could safely be disregarded in the numerical iteration. Of course  $m_j^{\text{max}}$  is chosen depending on the model parameters and the observable under investigation.

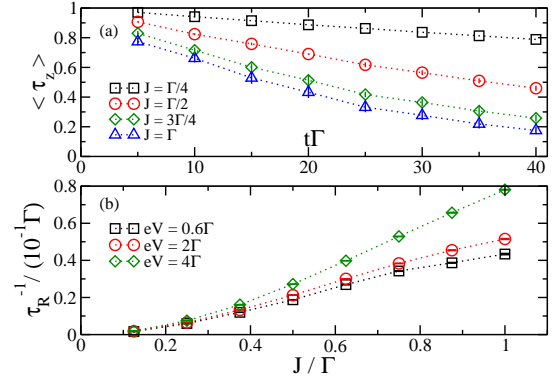


**Figure 14** (a) The expectation value  $\langle \tau_z \rangle$  of the impurity orientation as a function of propagation time for different strengths  $J$  of an anti-ferromagnetic electron-impurity interaction. The initial preparation of the system at  $t = -\infty$  is spin-up [ $\tau_z(0) \equiv \tau_i = 1$ ], for the other parameters see text. The polarization decays faster with increasing  $J$ . (b) Impurity relaxation rate  $\tau_R^{-1}$  as a function of the exchange coupling strength. Again the relaxation is faster with increasing coupling strength. In both panels the temperature is  $T = \Gamma$ .

Rapidly decreasing weights of the paths may not be (over-)compensated by their increasing numbers for  $0 \leq m_j \leq K-1$ , since each contribution is small and the number of paths decreases again for larger  $m_j \geq K$ . The behavior of the impurity weights is illustrated as follows. Consider the case when  $m_j$  is close to the maximum  $2(K-1)$ . Both path classes with  $m_j = 0$  and  $m_j = 2(K-1)$  contain the same number of elements (four), while each path contribution in the second class is weighted by  $(J\delta_t/2)^{2(K-1)}$ . For typical values of  $K = 4$ ,  $\delta_t\Gamma = 1/2$ , and  $J = \Gamma$ , the weight is  $\sim 2.5 \times 10^{-4}$ . This also holds for all  $K \leq m_j \leq 2(K-1)$ . Since  $m_j^{\text{max}}$  is unknown *a priori*, we include it into our code as an additional parameter. Then, we perform a numerical estimate by a spot sample of the parameter space. It turns out that for the considered cases, it is sufficient already to choose  $m_j^{\text{max}} = 2$ . This drastically reduces the CPU running times from more than one month to typically three to five days.

**6.1 Impurity dynamics** We focus on transport features caused by the magnetic impurity in this section. We emphasize that novel dynamical and transport features are mediated by the transverse or flip-flop interaction  $H_{\text{int}}^\perp$ , given in Eq. (29). Without the possibility of flip-flops the orientation of the impurity spin and its quantum state could not change. The remaining longitudinal part  $H_{\text{int}}^\parallel$  of the interaction causes a renormalization of rates and energies which appears as effective magnetic field. Necessarily, flip-flop processes are involved from the beginning to investi-

gate the non-trivial impurity dynamics by considering the time dependence of the impurity orientation  $\langle \tau_z \rangle$ . In all presented results below, the impurity is fully polarized at  $t = -\infty$  and the coupling to the leads is switched on.

In Fig. 14 (a) we present the time evolution of the impurity polarization  $\langle \tau_z \rangle$  for different values of the exchange interaction  $J$ . The remaining parameters are  $\Phi_D = \Delta = \Delta_{\text{imp}} = U = 0$ , and  $T = \Gamma$  and  $eV = 0.6\Gamma$ . The impurity polarization shows a clear exponential decay  $\langle \tau_z \rangle(t) \propto e^{-(t-t_i)\tau_R^{-1}}$ , well described by a single relaxation rate for intermediate to long propagation times. A faster decay is observed as the impurity interacts stronger with the electron spins. The parameters are chosen to yield an isotropic (symmetric with respect to [relative] spin orientations) model system. In this case the antiferromagnetic interaction favors antiparallel orientation of electron- and impurity spin. Over long propagation times, the coupling to the unpolarized leads then destroys any polarization of the impurity. It is therefore reasonable to assume, that the rates for up- and down flips are equal. While the impurity interaction energy is comparable to the tunneling coupling and considerably affects the transport behavior as we show below (see Fig. 15), the rather high temperature and bias voltage nevertheless reduce the relevance of coherent dynamics due to on-dot interactions to a secondary role.

We next investigate the relaxation rate  $\tau_R^{-1}$ . In Fig. 14(b) for  $T = \Gamma$ . We present results for varying  $J$  and  $U = 0$ , and three different bias voltages. These show a nearly quadratic behavior growing from zero (no relaxation) in the sense that for a fit of the results for  $0 \leq J \leq \Gamma/2$  to a polynomial function  $aJ^b$  the exponent  $b$  lies between  $\sim 1.8$  and  $\sim 1.9$ . An *exact* quadratic dependence of  $\tau_R^{-1}$  on  $J$  is obtained only when the dynamics is *strongly* dominated by sequential (incoherent) flip-flop processes [74]. This is only realized when  $J \ll \Gamma$ . A sequential flip-flop process consists of three elementary components: the actual flip-flop and two tunnelling processes of single electrons with opposite spins (not necessarily in that order). Since they evolve coherently, these components form an effective spin-flip process  $|\chi, \tau\rangle \rightarrow |\chi, -\tau\rangle$ , where  $\chi \in \{0, \sigma, d\}$  and the underlying flip-flop nature is masked by the tunnelling electrons.

**6.2 Charge current for finite impurity interaction and Coulomb repulsion** In the deep quantum regime, where no small parameter exists, ISPI is able to describe physical properties not predictable by perturbative methods. In this section, we study how the current behaves as functions of bias voltage, Coulomb interaction and temperature, respectively.

Fig. 15 (a) shows that the flip-flop term  $H_{\text{int}}^{\perp}$  has a considerably smaller influence on the charge current at  $T = \Gamma$  (incoherent regime) than the longitudinal part of the interaction in Eq. (29). Despite the qualitatively similar behavior of the Landauer-Büttiker (LB) current and the exact data, the flip-flop scattering causes an additional significant current drop that grows for growing  $J$ . A finite Coulomb

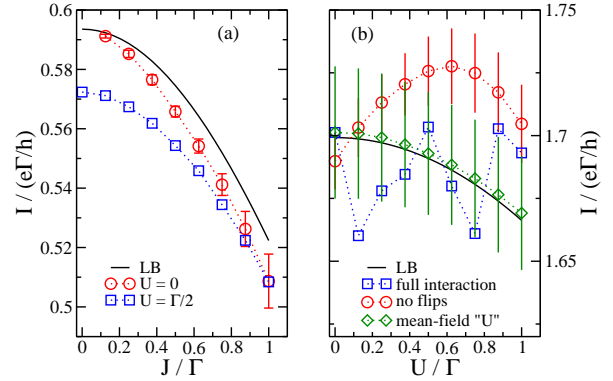


**Figure 15** (a) Charge current as a function of the exchange interaction  $J$  for two values of the on-dot interaction  $U$  at  $T = \Gamma$  and  $eV = 0.6\Gamma$ . The solid line marks the Landauer-Büttiker result, where exchange correlations are treated on a mean field level, see Ref. [74]. (b) Comparison of (i) the LB current (solid lines), (ii) the Coulomb interacting current without flip-flop scattering (“no flips”, red circles), (iii) the current without Coulomb scattering but full impurity interaction (“mean-field  $U$ ”, green diamonds, see the text for explanation), and (iv) the fully interacting current (“full int.”, blue squares) in their dependence on the Coulomb interaction  $U$  for  $T = \Gamma$ . The other (non-zero) parameters are  $J = \Gamma$  and  $eV = 2\Gamma$ .

interaction of  $U = \Gamma/2$  increases the resistivity of the dot and the ISPI points are consistently lower than the LB values. The voltage is chosen as  $eV = 0.6\Gamma$ . In Fig. 15 (b), for  $T = \Gamma$  four different current curves are shown—one for each possibility to either have (i) only mean field dynamics, regarding  $J$  (LB), (ii) the full Coulomb interaction without flip-flop processes (“no flips”), (iii) flip-flop dynamics without Coulomb fluctuations (“mean-field  $U$ ”), and (iv) the fully interacting dot (“full int.”). For  $J = \Gamma$  and  $V = 2\Gamma$ , the Coulomb energy is varied between  $0 \leq U \leq \Gamma$ . The situation “mean-field  $U$ ” is implemented by setting  $\Phi_D = U/2$  and the HS parameter  $\lambda = 0$  to illustrate the effect of the “classical” part of the Coulomb interaction. Only for the “single-interaction” currents (“no flips”), we show the error bars. We do not show a margin of confidence for the fully interacting case in order that the error data remain comparable. Calculating the “full int.” current is a time consuming task and thus, the extrapolation involves considerably fewer data points. Nevertheless, this does not render these values unreliable (we still see a compelling linear behavior of the  $1/\tau_c$  extrapolation with errors of the order of 1% based on the sample standard deviation). Both the mean-field current and the current without Coulomb scattering show only a weak dependence on

$U$  due to the single-particle energy shift. The current with full Coulomb interaction but fixed impurity shows a local maximum for  $U \sim \Gamma/2$ . In this case, the fixed impurity acts as an effective static magnetic field. The ISPI values for the fully interacting dot vary strongly over the considered  $U$  interval, but are scattered around the “no flips” and “mean-field  $U$ ” curves.

As long as the Coulomb interaction is small, differences in the data arise from including or excluding flip-flop processes. Hence, the rather good agreement of the  $U = 0$  values suggests that even at this, temperature flip-flop processes alone affect the current only weakly. Nevertheless, for decreasing temperatures, the flip-flop processes start to influence the current more strongly, which results in an increased resistivity. The case of the “no flip” current (fixed impurity) is equivalent to a Coulomb-interacting single-level quantum dot in a magnetic field. This effect is caused by the broadening of the dot’s joint density of states due to the Coulomb fluctuations.

**7 Conclusions** In summary, we have reviewed a scheme for the iterative summation of real-time path integrals (ISPI) and applied it to prototypical problems of quantum transport through an interacting quantum dot coupled to metallic leads held at different chemical potentials. After integrating over the leads’ degrees of freedom, a time-nonlocal Keldysh self-energy arises. Exploiting the exponential decay of the time correlations at finite temperature allows us to introduce a memory time  $\tau_c$  beyond which the correlations can be truncated. Within  $\tau_c$ , correlations are fully taken into account in the corresponding path integral for the Keldysh generating function. Then, through a discrete Hubbard-Stratonovich transformation, interactions are transferred to an auxiliary spin field, and an iterative summation scheme is constructed. The remaining systematic errors due to the finite time discretization and the finite memory time  $\tau_c$  are eliminated by a refined Hirsch-Fye-type extrapolation scheme, rendering the ISPI numerically exact.

The scheme has been applied to the canonical example of a single-impurity Anderson dot with Coulomb interaction  $U$ . This allows us to carefully and systematically check the algorithm. For linear transport, we have recovered results from second-order perturbation theory in  $U$  in the limit of very small interaction strength, but found significant deviations already for small-to-intermediate values of  $U$ . In the incoherent sequential regime, we recover results from a master equation approach. We have furthermore reproduced the linear conductance above the Kondo temperature. In addition, we have investigated the regime of correlated nonlinear transport, where, in our opinion, the presented method is most valuable. The *nonequilibrium* Kondo regime, representing an intermediate-to-weak coupling situation, seems tractable by the ISPI scheme.

Our approach is, in fact, similar in spirit to the well-established concept of the quasi-adiabatic path integral

(QUAPI) scheme, introduced by Makri and Makarov [89] in its iterative version. This method has been developed to describe the dynamics of a quantum system coupled to bosonic environments, see also Refs. [70,90].

In a second example, we have applied the ISPI technique to the spinless Anderson-Holstein model as well, which is the simplest nonequilibrium model for molecular quantum dots with a phonon mode. Our formulation exploits a mapping to an effective three-state system and reproduces three analytical theories valid in different parameter regions. This extension of the ISPI approach then captures the full crossover between those limits. For strong electron-phonon coupling and a nonequilibrated phonon mode, we find that the Franck-Condon blockade becomes even more pronounced as one enters the deep quantum coherent regime.

The complex system of an incorporated spin-1/2 magnetic impurity in a quantum dot has been subject of a third study, focusing on the real-time dynamics in the presence of Coulomb interactions. We include the impurity interaction on the same level as the other interactions, which results in an additional sum over impurity paths. An efficient truncation scheme nevertheless provides accurate results for the coupled spin dynamics. Results are given for a quantum spin-1/2 impurity on the dot, whereas the generalization to an impurity with a larger spin is possible. For a small impurity interaction, where sequential flip-flops dominate the impurity dynamics, we have found good agreement with a classical rate equation, see Ref. [74] as well. This is a useful tool to gain insight into the dominating processes in the incoherent regime. Relaxation is described reasonably well by a rate equation when lead-induced coherences are absent.

In the deep quantum regime, however, we find that the ISPI method is the only tool to obtain both the correct order of magnitude and the qualitative features of the relaxation rate as it depends on the system parameters  $U$  and  $J$ . The same holds for the influence of  $J$  and  $U$  on the current in this interesting corner of the parameter space. Most importantly, the ISPI scheme proves to be useful to cover the full cross-over regime where no small parameter exists and thus any perturbative approach becomes invalid.

We have provided a first glimpse on the interesting new physics that comes into reach with the ISPI scheme. Compared to other approaches, it has several advantages (e.g., numerical exactness, direct nonequilibrium formulation, no sign problem), but is, on the other hand, computationally more costly than most other techniques, especially for strong correlations and/or low energy scales (temperature, voltage).

**Acknowledgements** Financial support by the DFG through SPP 1243 “Quantum transport at the molecular scale”, DFG SFB 668 “Magnetismus vom Einzelatom zur Nanostruktur” and DFG project KO 1987/5 (SW) is acknowledged. Computational time from the ZIM at Heinrich-Heine Universität Düsseldorf with support from S. Raub is greatly acknowledged.



## References

- [1] T. Heinzl, *Mesoscopic Electronics in Solid State Nanostructures*, 2nd ed. (VCH-Wiley, Berlin, 2006).
- [2] J.C. Cuevas and E. Scheer, *Molecular electronics: An Introduction to Theory and Experiment* (World Scientific, Singapore, 2010).
- [3] *Introducing Molecular Electronics*, G. Cuniberti, G. Fagas, K. Richter (eds.), Lecture Notes in Physics, (Springer, Heidelberg, 2005).
- [4] M. Galperin, M.A. Ratner, and A. Nitzan, *J. Phys. Cond. Matt.* **19**, 103201 (2007).
- [5] J. Reichert, R. Ochs, D. Beckmann, H. B. Weber, M. Mayor, and H. v. Löhneysen, *Phys. Rev. Lett.* **88**, 176804 (2002).
- [6] R. Smit, Y. Noat, C. Untiedt, N. D. Lang, M. C. van Hemert, and J. M. Ruitenbeek, *Nature* **419**, 906 (2002).
- [7] T. Böhler, J. Grebing, A. Mayer-Gindner, H. v. Löhneysen, and E. Scheer, *Nanotechnology* **15**, 465 (2004).
- [8] H. Park, J. Park, A.K.L. Kim, E.H. Anderson, A.P. Alivisatos, and P.L. McEuen, *Nature* **407**, 57 (2000).
- [9] J. König, J. Schmid, H. Schoeller, and G. Schön, *Phys. Rev. B* **54**, 16820 (1996).
- [10] Y. Meir and N.S. Wingreen, *Phys. Rev. Lett.* **68**, 2512 (1992).
- [11] S. Hershfield, J.H. Davies, and J.W. Wilkins, *Phys. Rev. B* **46**, 7046 (1992).
- [12] A. Oguri, *Phys. Rev. B* **64**, 153305 (2001).
- [13] A.A. Aligia, *Phys. Rev. B* **74**, 155125 (2006).
- [14] R.M. Konik, H. Saleur, and A. Ludwig, *Phys. Rev. B* **66**, 125304 (2002).
- [15] A. Kaminski, Yu.V. Nazarov, and L.I. Glazman, *Phys. Rev. B* **62**, 8154 (2000).
- [16] A. Rosch, J. Paaske, J. Kroha, and P. Wölfle, *Phys. Rev. Lett.* **90**, 076804 (2003).
- [17] H. Schoeller and J. König, *Phys. Rev. Lett.* **84**, 3686 (2000).
- [18] T.A. Costi, *Phys. Rev. B* **55**, 3003 (1997).
- [19] S.G. Jakobs, V. Meden, and H. Schoeller, *Phys. Rev. Lett.* **99**, 150603 (2007).
- [20] T. Fujii and K. Ueda, *Phys. Rev. B* **68**, 155310 (2003); *J. Phys. Soc. Jpn.* **74**, 127 (2005).
- [21] P. Schmitteckert, *Phys. Rev. B* **70**, 121302 (2004).
- [22] A.J. Daley, C. Kollath, U. Schollwöck, and G. Vidal, *J. Stat. Mech.: Theor. Exp.* P04005 (2004).
- [23] D. Lobaskin and S. Kehrein, *Phys. Rev. B* **71**, 193303 (2005).
- [24] N.A. Zimbovskaya and M.R. Pederson, *Phys. Rep.* **509**, 1 (2011).
- [25] M. Galperin, M.A. Ratner, and A. Nitzan, *J. Phys.: Cond. Matt.* **19**, 103201 (2007).
- [26] H.G. Craighead, *Science* **290**, 1532 (2000); M.L. Roukes, *Phys. World* **14**, 25 (2001).
- [27] O. Tal, M. Krieger, B. Leerink, and J.M. van Ruitenbeek, *Phys. Rev. Lett.* **100**, 196804 (2008).
- [28] G.A. Steele, A.K. Hüttel, B. Witkamp, M. Poot, H.B. Meerwaldt, L.P. Kouwenhoven, and H.S.J. van der Zant, *Science* **325**, 1103 (2009).
- [29] B. Lassagne, Y. Tarakanov, J. Kinaret, D. Garcia-Sanchez, and A. Bachtold, *Science* **325**, 1107 (2009).
- [30] R. Leturcq, C. Stampfer, K. Inderbitzin, L. Durrer, C. Hierold, E. Mariani, M.G. Schultz, F. von Oppen, and K. Ensslin, *Nature Phys.* **5**, 327 (2009).
- [31] A. K. Hüttel, B. Witkamp, M. Leijnse, M.R. Wegewijs, and H.S.J. van der Zant, *Phys. Rev. Lett.* **102**, 225501 (2009).
- [32] A. Mitra, I. Aleiner, and A.J. Millis, *Phys. Rev. B* **69**, 245302 (2004).
- [33] H. Wang and M. Thoss, *J. Chem. Phys.* **131**, 024114 (2009).
- [34] S. Mackowski, T. Gurung, T.A. Nguyen, H.E. Jackson, L.M. Smith, G. Karczewski and J. Kossut, *Appl. Phys. Lett.* **84**, 3337 (2004).
- [35] A. O. Govorov and A.V. Kalameitsev, *Phys. Rev. B* **71**, 035338 (2005).
- [36] S.J. Cheng and P. Hawrylak, *Europhys. Lett.* **81**, 37005 (2008).
- [37] D.E. Reiter, T. Kuhn and V. M. Axt, *Phys. Rev. Lett.* **102**, 177403 (2009).
- [38] I. Zutic and A. Petukhov, *Nat. Nanotechnol.* **4**, 623 (2009).
- [39] C. Le Gall, R.S. Kolodka, C.L. Cao, H. Boukari, H. Mariette, J. Fernández-Rossier and L. Besombes, *Phys. Rev. B* **81**, 245315 (2010).
- [40] S.T. Ochsenein, Feng Yong, K.M. Whitaker, E. Badaeva, W.K. Liu, X. Li and D.R. Gamelin, *Nat. Nanotechnol.* **4**, 681 (2009).
- [41] Y. Léger, L. Besombes, J. Fernández-Rossier, L. Maingault and H. Mariette, *Phys. Rev. Lett.* **97**, 107401 (2006).
- [42] J. Fernández-Rossier and Ramón Aguado, *Phys. Rev. Lett.* **98**, 106805 (2007).
- [43] R. Hanson and D.D. Awschalom, *Nature* **453**, 1043 (2008).
- [44] P.S. Cornaglia, H. Ness, and D.R. Grempel, *Phys. Rev. Lett.* **93**, 147201 (2004).
- [45] L. Arrachea and M.J. Rozenberg, *Phys. Rev. B* **72**, 041301(R) (2005).
- [46] E. Gull, A.J. Millis, A.I. Lichtenstein, A.N. Rubtsov, M. Troyer, and P. Werner, *Rev. Mod. Phys.* **83**, 349 (2011).
- [47] A. Oguri, H. Ishii, and T. Saso, *Phys. Rev. B* **51**, 4715 (1995).
- [48] X. Wang, C.D. Spataru, M.S. Hybertsen, and A.J. Millis, *Phys. Rev. B* **77**, 045119 (2008).
- [49] L. Mühlbacher and E. Rabani, *Phys. Rev. Lett.* **100**, 176403 (2008).
- [50] M. Schiró and M. Fabrizio, *Phys. Rev. B* **79**, 153302 (2009).
- [51] J.E. Han, *Phys. Rev. B* **81**, 113106 (2010), J.E. Han and R.J. Heary, *Phys. Rev. Lett.* **99**, 236808 (2007).
- [52] A. Dirks, P. Werner, M. Jarrell, and T. Pruschke, *Phys. Rev. E* **82**, 026701 (2010).
- [53] S. Weiss, J. Eckel, M. Thorwart, and R. Egger, *Phys. Rev. B* **77**, 195316 (2008); *ibid.* **79**, 249901(E) (2009).
- [54] D.A. Abanin and L.S. Levitov, *Phys. Rev. Lett.* **94**, 186803 (2005).
- [55] A. Mitra, and A.J. Millis, *Phys. Rev. B* **76**, 085342 (2007).
- [56] D. Segal, A.J. Millis, and D.R. Reichman, *Phys. Rev. B* **82**, 205323 (2010).
- [57] P.W. Anderson, *Phys. Rev.* **124**, 41 (1961).
- [58] H. Bruus and K. Flensberg, *Many-Body Quantum Theory in Condensed Matter Physics*, (Oxford UP, Oxford, 2004).
- [59] A. M. Tselik and P. B. Wiegmann, *Adv. Phys.* **32**, 453 (1983).
- [60] A. Schiller and S. Hershfield, *Phys. Rev. B* **51**, 12896 (1995).
- [61] B. Horvath, B. Lazarovits, O. Sauret, and G. Zarand, *Phys. Rev. B* **77**, 113108 (2008).

- [62] L.V. Keldysh, Zh. Eksp. Teor. Fiz., **47**, 1515 (1964) [Sov. Phys. JETP **47**, 804 (1961)].
- [63] J. Rammer and H. Smith, Rev. Mod. Phys. **58**, 323 (1986).
- [64] A. Kamenev, in *Nanophysics: Coherence and Transport*, Les Houches session LXXXI, ed. H. Bouchiat, Y. Gefen, S. Guéron, G. Montambaux, and J. Dalibard (Elsevier, New York, 2005).
- [65] J.W. Negele and H. Orland, *Quantum Many-Particle Systems* (Addison-Wesley, Redwood City, 1988).
- [66] J.E. Hirsch, and R.M. Fye, Phys. Rev. Lett. **56**, 2521 (1986).
- [67] J.E. Hirsch, Phys. Rev. B **28**, 4059 (1983).
- [68] R.M. Fye, Phys. Rev. B **33**, 6271 (1986).
- [69] H. De Raedt, and B. De Raedt, Phys. Rev. A **28**, 3575 (1983).
- [70] J. Eckel, S. Weiss, and M. Thorwart, Eur. Phys. J. B **53**, 91 (2006).
- [71] J. Hubbard, Phys. Rev. Lett. **3**, 77 (1959).
- [72] F. Siano and R. Egger, Phys. Rev. Lett. **93**, 047002 (2004).
- [73] R. Hützen, S. Weiss, M. Thorwart, and R. Egger, Phys. Rev. B **85**, 121408(R) (2012).
- [74] D. Becker, S. Weiss, M. Thorwart and D. Pfannkuche, New J. Phys. **14**, 073049 (2012).
- [75] J. Eckel, F. Heidrich-Meisner, S.G. Jakobs, M. Thorwart, M. Pletyukhov, and R. Egger, New J. Phys. **12**, 043042 (2010).
- [76] L. Dell'Anna, A. Zazunov, and R. Egger, Phys. Rev. B **77**, 104525 (2008).
- [77] T.A. Costi, A.C. Hewson, and V. Zlatic, J. Phys.: Condens. Matter **6**, 2519 (1994).
- [78] F. Heidrich Meisner, A.E. Feiguin, and E. Dagotto, Phys. Rev. B **79**, 235336 (2009).
- [79] D.R. Hamann, Phys. Rev. **158**, 570 (1967).
- [80] Yu.V. Nazarov and Ya.M. Blanter, *Quantum Transport* (Cambridge University Press, 2010).
- [81] A. Kamenev and A. Levchenko, Adv. Phys. **58**, 197 (2009).
- [82] R. Egger and A.O. Gogolin, Phys. Rev. B **77**, 113405 (2008).
- [83] B. Dorá and A. Halbritter, Phys. Rev. B **80**, 155402 (2009).
- [84] Y. Vinkler, A. Schiller, and N. Andrei, Phys. Rev. B **85**, 035411 (2012).
- [85] S. Braig and K. Flensberg, Phys. Rev. B **68**, 205324 (2003).
- [86] J. Koch and F. von Oppen, Phys. Rev. Lett. **94**, 206804 (2005).
- [87] F. Pistolesi, Ya.M. Blanter, and I. Martin, Phys. Rev. B **78**, 085127 (2008).
- [88] N. Bode, S. Viola Kusminskiy, R. Egger, and F. von Oppen, Phys. Rev. Lett. **107**, 036804 (2011).
- [89] D.E. Makarov and N. Makri, Chem. Phys. Lett. **221**, 482 (1994); N. Makri and D.E. Makarov, J. Chem. Phys. **102**, 4600 (1995); N. Makri and D.E. Makarov, J. Chem. Phys. **102**, 4611 (1995); N. Makri, J. Math. Phys. **36**, 2430 (1995).
- [90] M. Thorwart and P. Jung, Phys. Rev. Lett. **78**, 2503 (1997); M. Thorwart, P. Reimann, P. Jung, and R.F. Fox, Chem. Phys. **235**, 61 (1998).